JOURNAL OF PROPULSION AND POWER
Vol. 14, No. 3, May–June 1998

Surface Modification Measurements in the T5 Ion Thruster Plume

L. Najeeb Ahmed* and Mark W. Crofton†
The Aerospace Corporation, El Segundo, California 90245-4691

The measurement and analysis of thruster-induced surface modifications of a variety of materials in the T5 (UK-10) xenon ion engine environment has been performed. Surface modification because of impinging contaminants in the thruster ground-test environment was studied for about 50 collimated spacecraft material samples at fixed sites, including solar cells, paints, and optical solar reflectors. Emittance and solar absorptance properties were determined pretest and posttest. Elemental composition was determined for the deposition surface layers accumulated during the 65-h exposure of the various samples, to obtain mass deposition rates for individual elements. While a number of samples acted as simple sputter monitors, behavior of the paints was complex, showing strong dependence of posttest surface deposition layer on paint chemistry. Angular distributions of the total mass deposition rate were obtained with a rotatable, collimated quartz crystal microbalance (QCM). Results from most samples and the QCM show increasing deposition of molybdenum with increasing observation angle. Deposition increased rapidly from 20 to 35 deg off the grid plane, and observed deposition rate peaked at approximately 45 deg. The variation of deposition rate with accelerator and decelerator grid voltages, propellant mass utilization, and facility background pressure was also investigated. The results are relevant to the impact of thruster operation on spacecraft surfaces and the evaluation of thruster grid lifetime as a function of operating point.

Nomenclature

A = quartz crystal microbalance crystal area exposed to mass flux
F = flow rate of xenon propellant
I_{acc} = accelerator grid current
I_b = beam current
I_{dec} = decelerator grid current
j_{ce} = production rate of charge exchange ions
j_{dr} = deposition rate
n_i = Xe^+ density
n_0 = xenon neutral density
S = quartz crystal microbalance mass sensitivity, g cm^{-2} Hz^{-1}
V_a = anode voltage
V_{acc} = acceleratorerator grid voltage
V_b = beam voltage, screen voltage
V_{dec} = deceleratorerator grid voltage
α = absorptance
α_s = solar absorptance
α_λ = absorptance at wavelength λ
Δf = change in beat frequency
ΔM = change in mass
ε_h = hemispherical emittance
ε_λ = emittance at wavelength λ
η_m = mass utilization efficiency
θ = angle from decelerator grid exit plane
ν_i = Xe^+ velocity
ρ = reflectance
σ_{ce} = charge exchange cross section
τ = transmittance

Received Aug. 21, 1995; revision received Dec. 16, 1997; accepted for publication Dec. 28, 1997.

*Lieutenant, U.S. Air Force, Education With Aerospace Program; currently Captain, U.S. Air Force, F16 System Program Office, ASC/YPX, 1981 Monahan Way, Wright–Patterson Air Force Base, OH 45433-7542.

†Senior Member, Technical Staff, Technology Operations, Mechanics and Propulsion Department, M5-754, P.O. Box 92957, Los Angeles, CA 90009-2957. Member AIAA.

Introduction

APPLICATION of ion propulsion devices for auxiliary propulsion raises concerns about unforeseen risks. The primary advantage of ion engine propulsion is a reduction in propulsion system wet mass for many missions, which can be used to improve payload effectiveness, extend satellite lifetime, and/or reduce launch costs.[1–3] Other potential benefits include reduced trip time for geosynchronous longitude shifting, improved accuracy of spacecraft pointing and stationkeeping, and greater allowance for unanticipated maneuvering.[4] On the other hand, ion engines carry a higher risk than several alternatives with lower performance specifications, because of more limited flight experience.[5]

An ion thruster interacts with its host spacecraft and the surrounding space plasma. The impingement of neutral and ionized atoms originating from the thruster is the primary means by which optical, thermal, and other properties of spacecraft surface materials are modified. Results of the present study, which investigates the surface modification for a variety of materials in the thruster-induced environment, apply specifically to the British T5 ion engine, but are of general importance for the integration of electrostatic gridded ion engines.

Spacecraft surface contamination is a critical issue that can affect the performance of both the spacecraft and its payload. Thruster-induced contamination has been an occasional problem even for chemical thruster systems, which are generally less prone to these effects. NASA's Long Duration Exposure Facility (LDEF) exposed many different types of materials to surface modification effects in space on a platform designed to accommodate technology, science, and applications experiments measuring the effects of long-term exposure to the space environment.[6]

A number of previous studies have examined the thruster lifetime and spacecraft contamination issues associated with mercury ion engines[7,8] before the international changeover to

Table 1 Exposure test parameters[a]

Day	Beam hours	Hours at I_b = 457 mA	Equilibrium I_{acc}, mA	Equilibrium I_{dec}, mA	Equilibrium V_{ca} anode voltage	Hours at $I_{dec} \geq 1.2$ mA
1	2.8	2.8	1.19	0.96	43.2	0.5
2	7.3	7.3	1.18	0.92	43.4–44.0	0.4
3	11.6	11.6	1.16–1.21	0.87–0.92	43.5–44.5	0.15[b]
4	12.6	12.4	1.16–1.21	0.88–0.91	43.4–44.3	0.5
5	12.1	11.3[c,d]	1.14[f]–1.28[e]	0.86[f]–0.96	42.5[e]–44.6[f]	0.3
6[g]	7.6	7.2	1.16–1.20	0.41[h]–0.93	43.9–44.4[f]	0.1
7	10.7	10.7	1.25–1.32	0.46[h]–0.65	42.8–43.6	0.0

[a]Anode (discharge) current = 3.02 A, cathode keeper current = 0.5 A, cathode keeper voltage = 10.5 V, magnet current = 150 mA, accel grid at −225 V, decel grid at −50 V, V_b = 1100 V, nominal η_m = 89 ± 2%. Flow rates were measured by rate of pressure rise in a known volume, with thruster off, to an accuracy of about 2%. All η_m values given in this study neglect neutralizer flow.
[b]28-min delay between start of main discharge and beam.
[c]Thruster was operated in the I_b = 420–456-mA range for 0.8 h to control decel grid current.
[d]During several hours of unsupervised operation, η_m climbed by several percent and beam extraction was lost for nearly an hour.
[e]The flow rate was increased slightly after the event described in note c. During the cool evening hours the utilization dropped further.
[f]Estimated parameter.
[g]Room temperature was as high as 30°C on this day because of lack of air conditioning, causing reduced propellant flow rate and a recycle event.
[h]The decel current dropped dramatically toward the end of day 6; it remained low on day 7, it is not understood why this occurred.

xenon propellant. Several flight tests of mercury ion thrusters have been conducted, of which the most important was the SERT II experiment.[9]

Development of xenon ion engines has accelerated recently, with several experimental and operational uses planned. Although short-duration flight operations involving xenon ion engines have been conducted,[10,11] the Hughes XIPS-13 engine is the first gridded ion thruster to enter routine operational service (1997).[12]

A 500-h test on a T5 xenon ion thruster, in two- and three-grid configurations, found the erosion rate of the accelerator grid to be the life-limiting component of the thruster.[13,14] In that study, witness plate deposits were analyzed and fixed quartz crystal microbalance (QCM) measurements were made during the test. Laser spectroscopic measurements of molybdenum atom density in the plume as a function of operating point have been made for T5[15] and XIPS-13[16] thrusters. Contamination characteristics of a 30-cm xenon ion engine are under investigation for the NSTAR spacecraft.

Experiments detailed in the present study[17] were performed to re-examine the interaction between thruster plume and sample spacecraft materials as a function of spatial coordinate. Total mass deposition rates were measured using a QCM, and emittance and absorptance property changes as well as surface-layer elemental composition were determined following a controlled exposure of 49 witness samples.

Test Configuration

The test article was an engineering model British ion thruster, designated T5 Mk3, operating on xenon propellant. A flight version incorporating several design improvements and the necessary subsystems is known as the UK-10 ion propulsion system. The T5 was configured with a triple grid set of similar design to that now slated for use on the Advanced Relay and Technology Mission (ARTEMIS) but differing in several important respects.[18] Flight hardware was not available. The decelerator grid had a thickness of 0.75 mm, and the accelerator–decelerator separation was 1.0 mm at center, large enough to lead to substantial direct impingement of beamlet ions under some conditions. Screen grid and accelerator grid thicknesses were 0.25 and 0.75 mm, respectively. Details of the T5 design may be found elsewhere.[19]

Experimental testing was performed in a test chamber 5.5 m in length and 2.4 m in diameter. Two custom 1.2-m CVI re-entrant cryopumps of combined ~70,000-l/s pumping speed on xenon hung inside the chamber, suspended from flanges.

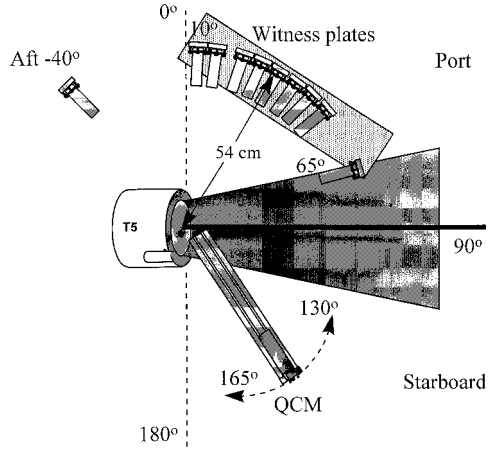

Fig. 1 Typical location of rotatable quartz crystal microbalance and fixed-position materials samples with respect to the T5 thruster. The angle θ, given at several positions, is referenced to a plane intersecting the centerpoint of the inwardly dished decelerator grid and perpendicular to the grid axis.

During thruster operation at a nominal thrust level of 25 mN, the chamber pressure was maintained at 2×10^{-6} torr.

Table 1 indicates the test parameters during a 65-h exposure of spacecraft materials samples to the thruster environment. The QCM measurements were obtained before and after the sample exposure period.

Because of the marginal supply rate of liquid nitrogen to the cryopump shrouds, chamber pressure as high as 2.7×10^{-6} torr occurred on some days after 8 h of continuous operation. The thruster was mounted on a fixed stand in a side chamber with the ion beam directed across the main chamber. All plume measurements were taken at 54 cm distance from the decelerator grid centerpoint. Rotatable platform mounting of the QCM permitted positioning over angular ranges θ = 8–55 and 130–165 deg, 54 cm downstream from the decelerator center. Various spacecraft materials were stationed along the arc θ = 10–50 deg, with additional samples stationed at the edge of the engine plume field at 65 deg, and aft of the thruster at −40 deg (Fig. 1).

Mass Flux Measurements

Mass deposition rates measured as a function of plume coordinate, ion beam current, vacuum chamber background pres-

sure, and extraction grid voltages were accomplished with the use of a collimated quartz crystal microbalance. The 15-MHz QCM, supplied by QCM Research, had a mass sensitivity S of 1.96×10^{-9} g/cm^2-Hz, with exposed sense crystal and shielded reference crystal mounted in a stainless-steel module. The change in beat frequency between sense and reference crystals is related to QCM signal output by the relation $\Delta f = \Delta M/SA$.

The QCM was collimated to improve the precision of its measurements. Data taken at high angles with respect to the thruster axis could be affected by material sputtered from vacuum chamber walls. To reduce this as a possible source of contamination, a 3.2 × 10.2 cm aluminum collimator, designed for the 54-cm radial distance, was lined with tantalum foil and attached to the QCM. The single-aperture collimator was designed using ray tracing to view an area slightly larger than the grids at $\theta = 90$ deg (see Figs. 1 and 2).

Spacecraft Materials

To investigate the effects of the thruster plume on various spacecraft materials, an array of samples was mounted about the thruster. Constrained to positions similar to those where QCM mass flux measurements were taken, each sample-holder assembly provided five collimated stations for exposure to the thruster-induced environment, as shown in Fig. 3. Additional samples were placed in regions not explored by the QCM, near the core of the engine plume (65 deg), and aft of the grid plane (−40 deg).

The samples were mounted between two aluminum plates, with O-rings on either side to secure their positions in the assembly without damage. The center position of each assembly, station 3, was in the horizontal plane of QCM rotation and of the thruster (containing the decelerator centerpoint). Those materials on either end of the assembly, the top (station 1) or the bottom (station 5), were properly adjusted to maintain their line of sight with the thruster. Samples placed in station 3 were 54 cm from the decelerator grid center. Samples placed in stations 1 and 5 viewed the grid center from ~9 deg off the horizontal plane and 0.6 cm greater distance. Because of the high radial symmetry observed in the T5 ion beam and the small variation of viewing distance and viewing angle on the station number of individual samples, the effect of the station number on the sample environment was assumed to be insignificant. Table 3 of Ref. 17 relates the position of each of the samples within the witness plate assembly.

The 49 samples exposed to the engine plume were representative of typical materials found on spacecraft. These materials may be divided into three groups: solar absorbers, white paints, and solar reflectors, as shown in Table 2, members of each class having similar functions.

The CMX samples were cerium dioxide-doped borosilicate glass with an indium–tin–oxide (ITO) conductive coating on the front surface to reduce static buildup. Details of spacecraft materials properties and functions may be found elsewhere.[20]

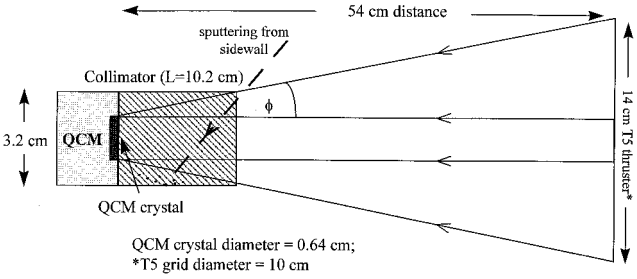

Fig. 2 Collimator ray-tracing diagram.

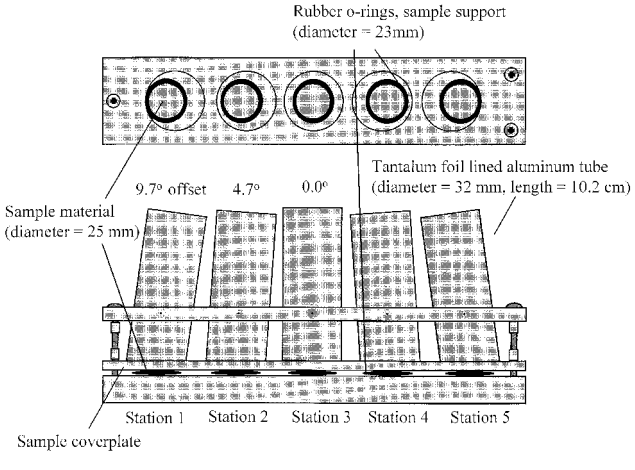

Fig. 3 Sample holder assembly.

Procedure

Quartz Crystal Microbalance

Trial runs were made to determine an appropriate duration for QCM bakeout prior to each day's measurements and the wait interval following repositioning from one viewing angle to another. Although the QCM was designed to minimize temperature effects, it was found that the QCM signal was clearly dependent on the thermal characteristics of the object in view. With grid voltages off, the equilibrium beat frequency varied substantially for many minutes after the main discharge or neutralizer was switched off and also when the viewing angle was altered. To investigate the QCM response a number of mass gain dependence vs location plots were generated at various operating points. It was found that a 15-min time interval was necessary for the QCM to reach stability after being repositioned. As seen in Fig. 4, a substantial drift in the QCM signal is evident during this 15-min period. The pretest results were used to block out regions of the data file where mass flux measurements were likely to be affected by a change in settings.

A typical QCM data run started with an initial 120-min pretest delay, to bakeout contaminants from the sense crystal at 80°C. This was followed by another 60-min delay, to drop the unit's temperature to 60°C and stabilize it for data collection.

Table 2 Spacecraft materials samples exposed to the thruster environment

Solar absorbers:
(MH) MH21S/LO® black paint on 25-mm aluminum disk
(SC) Edmund Scientific SuperCell® Solar Cell, 2.5 × 6.2 cm
(K) Dupont Kapton® film, 0.05-mm on 25-mm aluminum disk
White paints:
(YB) YB-71/PS-7® white paint on 25-mm aluminum disk
(ZP3) Z93® white paint on 25-mm aluminum disk
(Z93P) Z93P® white paint on 25-mm aluminum disk
(S13) S13GP/LO-1® white paint on 25-mm aluminum disk
Solar reflectors (second-surface mirrors):
(CMX) indium-tin-oxide-(ITO-)coated CMX, 20 × 20 × 0.15 mm, Pilkington
(ST) silver teflon, FEP/Ag/Inconel, 0.13 mm on 25 mm aluminum disk
(OSR) fused silica optical solar reflectors, 40 × 20 × 0.20 mm

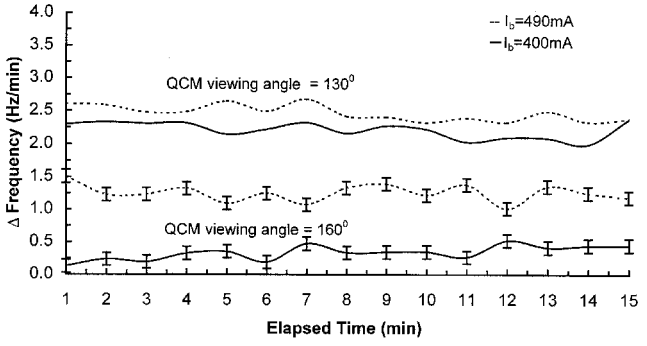

Fig. 4 Typical QCM settling behavior following repositioning.

A 15-min stabilization period accompanied each rotation of the unit. This was followed by an interval of about 10 min, when mass flux measurements were obtained.

Pretest Sample Calibration

Measurements were also made on unexposed sample materials to indicate variations within the batch of each material. Solar absorptance measurements were made on two sets of 10 samples, sets A and B, with a Perkin–Elmer Lambda 9 Spectrophotometer utilizing a wavelength range from 250 to 2500 nm. A small error in determination of the solar absorptivity constant α_s can result from the limited wavelength range.

Realizing there was very little variation between sets A and B of the test materials, as seen in Table 3, all remaining tests were carried out on set A. However, a slight discrepancy was noticed within the YB-71 and Z93P white paint samples, along with the solar cell samples. The batch variations within the white paints were attributed to surface damage and contamination from the machining process necessary to cut each sample to the appropriate size for testing. The solar cell discrepancy was attributed to the fact that the lot was military surplus, without detailed specifications and, therefore, subject to variation between samples. Having the benefit of two sets of measurements, an average was taken to be the actual pretest solar absorptance value for each of the materials.

Pretest emittance measurements were made on set A and an additional limited number of materials, set C. Values of normal emittance were determined using a Gier-Dunkle DB100 infrared reflectometer.[21] Hemispherical emittance values were calculated directly from normal emittance values using the theoretically and empirically derived correlation between hemispherical and normal emittance.[22] As seen in Table 3, there is very little variation between sets A and C; therefore, emittance pretest figures from set A were used for all 49 samples.

Pretest x-ray photoelectron spectroscopy (XPS) measurements of elemental surface composition were made on all samples from set A, excluding the solar cell, which was too large for introduction into the XPS analysis instrument.

Midtest Vacuum Exposure

Sample set C (consisting of MH, SC, K, S13, and ST), was introduced to the vacuum chamber to measure possible contamination effects from the chamber. All five samples were mounted in a sample holder (see Fig. 3) without collimators, during chamber pump-down, and left under cryopump vacuum ($\leq 2 \times 10^{-7}$ torr) for approximately 46 h. Solar absorptance and XPS measurements were then made on all samples, excluding the solar cell.

Pretest absorptance and XPS measurements were not obtained for sample set C. The midtest results from set C were therefore compared with pretest results obtained from sets A and B.

Averaged set A and B pretest measurements of solar absorptance were compared with similar measurements on set C after exposure to the vacuum environment (see Table 4).

Table 3 Pretest solar absorptance and emittance measurements

	α_s			ε_H	
Sample	Set A	Set B	Average	Set A	Set C
Solar absorbers:					
MH	0.968	0.970	0.969	0.827	0.828
SC	0.835	0.819	0.827	0.796	0.796
K	0.623	0.627	0.625	0.800	0.799
White paints:					
YB	0.146	0.168	0.157	0.834	——
Z93	0.128	0.129	0.129	0.867	——
Z93P	0.127	0.146	0.137	0.865	——
S13	0.216	0.213	0.215	0.844	0.847
Solar reflectors:					
CMX	0.102	0.098	0.100	0.773	——
ST	0.069	0.072	0.071	0.748	0.749
OSR	0.063	0.066	0.065	0.760	——

Table 4 Midtest solar absorptance analysis[a]

	α_s				
	MH	SC	K	S13	ST
Pretest	0.969	0.827	0.625	0.215	0.071
Midtest	0.969	0.812	0.664	0.210	0.075

[a]Pretest figures are average of set A and set B results; midtest figures are set C results.

All midtest solar absorptance figures were consistent with pretest results to within experimental error and expected sample variation, except for the Kapton film. XPS pretest results for set A (XPS pretest analysis was not performed on set B) and midtest results for set C were obtained (see Table 6 of Ref. 17). The Kapton results were again anomalous, with low concentrations of Cl, Na, and S showing up in the midtest sample. Because other samples did not show comparable contamination, it is believed that the vacuum exposure was not the source of these contaminants. The difference in S13GP/LO pretest and midtest XPS results can probably be attributed to the variation in the pigment-to-binder ratio between samples.

Duration Test

All samples were exposed to the ion thruster plume during normal beam extraction at a nominal 25-mN thrust level, for 65 h (see Table 1 for operating parameters). Because of a technical difficulty, QCM data collection could not be performed during the 65-h sample exposure period, and in any case would have been limited to the 130- to 165-deg range.

Posttest Analysis

Following the duration test all samples were removed from their holders and underwent analysis to determine absorptance, emittance, and elemental surface composition. These samples were exposed to the atmosphere for up to 1 week prior to the conclusion of analytical testing. Each solar cell was truncated to obtain a sample size suitable for the XPS instrument.

Results and Discussion

Mass Flux Measurements

Two series of mass flux QCM measurements were taken, separated by approximately 400 beam hours on the screen, accelerator, and decelerator grids, accumulated at widely varying operating points. The decelerator grid was the same one used in a prior 500-h triple grid lifetest.[13] The screen and accelerator grids, also operated previously, had a different history than the decelerator grid. They were operated over a range of operating points, with most of the elapsed time at a nominal 25-mN, 80–85% propellant mass utilization.

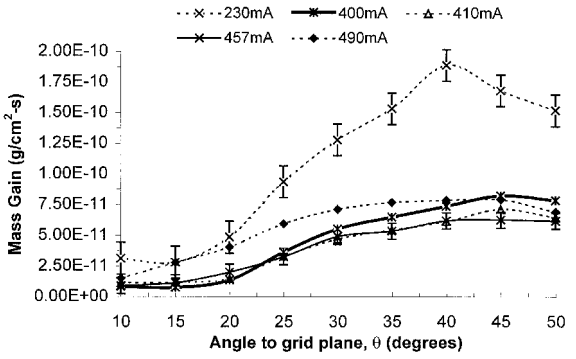

Fig. 5 Angular dependence of deposition rate measured by QCM for various beam current settings (F = 611-mA equivalent, V_{acc} = −225 V, V_{dec} = −50 V, V_b = 1100 V).

The 500-h lifetest results had indicated a very large decrease of QCM deposition and grid erosion rates with accumulated beam time. These rates were an order of magnitude lower at the conclusion of the lifetest than at the beginning.[13] Because the decelerator grid had been aligned and attached to the screen/accelerator grid assembly less than 50 beam hours prior to the start of our QCM testing, it was of value to measure and compare deposition rates, before and after a long interval, because of the possibility of ion machining.

The measurements investigated mass deposition rates as a function of angular coordinate, ion beam current, and extraction grid voltages. For historical reasons, the propellant mass utilization figures were quite different for the two series.

The first series of measurements was taken on the port side of the plume, and the second was taken on the starboard side (see Fig. 1) after the additional 400 h of accumulated beam time. Figure 5 shows a peak in mass deposition rate at about θ = 45 deg, regardless of beam current level. At $\theta \geq 50$ deg, QCM output was anomalous, exhibiting sudden frequency jumps during repositioning and the data acquisition period. This behavior was caused by the impingement of beam ions at extremely low flux levels relative to beam centerline. At ±40 deg (θ = 50 and 140 deg) from the beam axis the beam ion flux is down by a factor of about 5×10^{-5} for the 25-mN operating point.[23] The deposition flux at these angles corresponds to 4×10^{11} atoms cm^{-2} s^{-1}, assuming the mass deposit is entirely molybdenum. The ion flux, after applying the approximate inverse square correction for distance, is roughly 8×10^{11} cm^{-2} s^{-1} for a similar operating point. With a sputter yield of about 1 molybdenum atom/xenon ion at V_b = 1100 V,[24] erosion and deposition rates are comparable. The beam ion flux varies by more than an order of magnitude per 10-deg rotation in either direction, and varies with the operating point. The erosion rate is therefore dramatically lower at ±50 deg off the beam axis than at ±40 deg. Independent measurements of molybdenum density in the plume indicate it does not have a sharp angular dependence from 0 to 45 deg off-axis.[15] The expected distribution is a cosine function.[25] As a result, surface erosion strongly dominates for θ = 60–90 deg, whereas the deposition is dominant for $\theta \leq 50$ deg in Fig. 5.

For beam current levels in the 200–300-mA range, deposition rates were considerably higher. The total charge exchange ion production rate can be estimated from

$$j_{ce} = \int n_0 n_i \nu_i \sigma_{ce}\, dV \qquad (1)$$

where multiply charged ions have been ignored. Substantial variation of n_i and particularly n_0 occurs with spatial coordinate, ν_i varies in the intergrid region, and σ_{ce} is energy dependent. In the simplest picture, the maximum value of j_{ce} will occur at about 50% propellant mass utilization at a given F and ν_i, because the product of the average values of n_i and n_0 is highest for that operating point. 50% utilization corresponds to 305 mA for the data of Fig. 5. The maximum deposition rate actually occurred at a beam current of approximately 80 mA. This large discrepancy is believed to be a result of a defocusing effect associated with the ion extraction process at low beam currents. Analysis of the ion trajectories using a numerical modeling code,[26] high observed I_{dec} (2.5 mA) at I_b = 80 mA, and the plume density of sputtered molybdenum, directly measured over a wide range of beam current at constant F,[15] are all consistent with a direct impingement (DI) effect on the decelerator grid because of beamlet defocusing. Direct decelerator impingement would chamfer the downstream end of the aperture barrel, biasing the measured mass gain curve in Fig. 5 toward lower θ as observed for I_b = 230 and 490 mA.

The effect of beam voltage and vacuum chamber background pressure on the QCM signal at $\eta_m \sim 75\%$ was explored. The background pressure was elevated by bleeding xenon directly into the vacuum chamber. An ion gauge, known to have absolute accuracy better than ±30% on nitrogen, was corrected for xenon sensitivity. Figure 6 shows that the effect of background pressure was rather small up to 15×10^{-6} torr, with only a slight increase in the QCM signal. The rapid rise in decelerator current and relatively flat accelerator current was expected.[27] The sputter yield of molybdenum at 50-eV impact energy is very small, and triple-grid systems can operate with reduced accelerator and total grid erosion relative to twin-grid systems.

It was found that I_{dec} was a strong increasing function of I_b in the 420- to 457-mA range (23- to 25-mN nominal thrust). At about 450-mA beam current, an increase in beam voltage from 1100 to 1200 V had little effect on accelerator grid current but it did have a dramatic effect on decelerator current. At V_b = 1100 V, the onset of direct decelerator impingement occurred at about 450 mA. Decel current above 10 mA was observed for $I_b \geq 500$ mA. The elevated beam voltage was able to raise the onset of decelerator grid DI by about 40 mA. The threshold I_b associated with DI also increased with accumulated beam hours. After an additional 400 h of beam time, I_b = 457 mA at V_b = 1100 V was just above the threshold at normal operating temperature. A higher I_{dec} level was still observed during the 65-h test for more than 30 min after each start of beam extraction. A longer warm-up period with main discharge on but without the application of ion extraction voltages reduced the duration of high DI effects following beam turn-on.

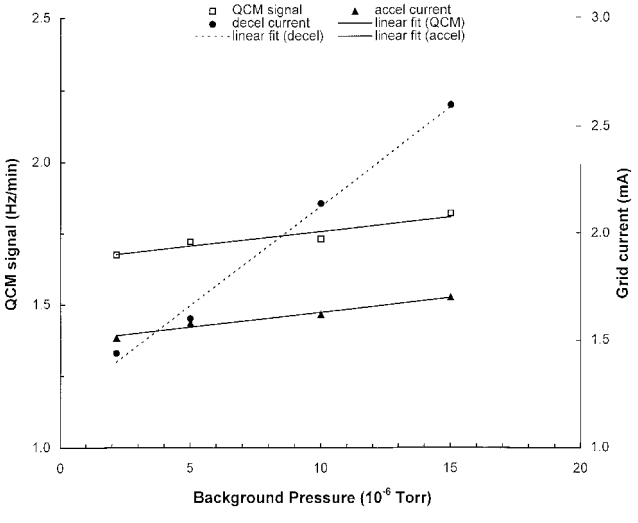

Fig. 6 Dependence of QCM signal, accelerator and decelerator grid currents on background pressure (θ = 40 deg, I_b = 457 mA, V_b = 1200 V, V_{acc} = −225 V, V_{dec} = −50 V, η_m = 75%).

The effect of extraction voltages on mass deposition rates was explored at the start of QCM testing and after 400 h of accumulated beam time. V_b and η_m differ in the two cases, but I_b was the same. Both data series show that an increase in absolute value of the decelerator grid voltage produces a small increase in deposition rate. This is accompanied in most cases by a substantial decrease in accelerator current and an increase in decelerator current (for example, in one case I_{acc}/I_{dec} = 1.74/1.27 mA at $V_{acc} = -300/V_{dec} = 0$ became 1.56/1.36 mA when V_{dec} was reset to -50). Because of a high redeposition factor for accelerator grids, decelerator current at a given impingement energy will produce considerably higher QCM mass gain. The decelerator voltage may influence the relative impingement probability on accelerator and decelerator grids of high-energy charge exchange ions formed in the intergrid region. While the $V_{dec} = 0$ operating point produces slightly less deposition material at spacecraft surfaces, the effect on accelerator grid lifetime is presumably negative because the grid current is higher.

The upper series of Fig. 7 clearly shows sharp increases in the deposition rate with an increasing absolute value of accelerator grid voltage. There is a dramatic difference in deposition rate j_{dr} dependence on accelerator grid voltage for the two data sets. The propellant mass utilization η_m was about 72% for the first (upper) series of QCM measurements in Fig. 7 and about 90% for the second. For a constant beam current, Eq. (1) predicts a deposition rate $\propto (1 - \eta_m)/\eta_m$, corresponding to a ratio of 3.5 between these cases if charge exchange erosion dominates. Dividing the series 1 curves in Fig. 7 by this factor, reasonable agreement is obtained for $V_{acc} = -400$ and -300, and a substantial discrepancy for $V_{acc} = -225$ (2.3×10^{-11} vs 1.2×10^{-11} g cm^{-2} s^{-1}). Examination of the grid currents indicates puzzling results, however, even for $V_{acc} = -400$. For the $V_{acc} = -400$, $V_{dec} = 0$ case, I_{acc} and I_{dec} were 1.82 and 1.33 mA, and 1.34 and 0.77 mA, respectively, for the low- and high-utilization figures. If the energy distribution of charge exchange ions was the same in the two cases and charge exchange erosion of the accelerator grid dominates the QCM mass gain, a ratio of about 4 between measured accelerator currents would have been expected at the two utilization figures. Complications include 1) DI effects (impingement at beam energies where a perveance limit has been reached), 2) the contribution to an observed QCM mass gain of molybdenum atoms derived from the screen grid and plume iron atoms from the thruster interior (see next section), 3) variation of impingement location and energy distribution on grid surfaces with η_m, and 4) the ion impingement contribution to the observed grid currents from processes independent of charge exchange (PIC ions) below the grid perveance limit. It does not appear that items (1) and (2) provide a complete explanation in this particular example. Iron accounts for only $\sim 5 \times 10^{-12}$ g cm^{-2} s^{-1}. Screen grid erosion also cannot provide an adequate explanation. As suggested by Fig. 6, charge exchange with background gas from the facility effect contributes little under normal operating conditions. Significant PIC or DI contributions would mean that 3 is an important factor. Also, in a ground test facility the ratio of charge exchange ions formed in the plume to those produced in the intergrid region depends on η_m.

While the dependence of j_{dr} on accelerator grid voltage is reasonable in the low η_m case according to known sputter yields, the high η_m case has the -225-V deposition rate above both -300- and -400-V rates. The implication is that decelerator DI effects are very significant when $V_{acc} = -225$ V and $V_b = 1100$ V at a nominal 25-mN thrust level. As a result, a properly designed grid set may be expected to achieve a plume deposition rate reduced by some 50% at a 25 mN, $\eta_m \sim 90\%$, $V_{acc} = -225$ V, $V_{dec} = -50$ V, $V_b = 1100$ V operating point, with further gains at lower beam voltage, as a result of a reduction in decelerator direct impingement. It was predicted in Ref. 17 that without DI effects on the decelerator, the QCM would have gained mass at the rate of about 1.8×10^{-11} g cm^{-2} s^{-1} at this operating point (including the contribution from iron), about half the observed rate. Newly designed grids employing straightforward improvements have been fabricated and tested.[28] The new test results show that this prediction was valid.

A substantial dependence of beamlet divergence on accelerator voltage was found in trajectory simulations, which was consistent with an increased DI effect for the $V_{acc} = -225$ V, $V_b = 1100$ V case, relative to the other operating points. Telemicroscopy data for the twin-grid configuration indicate that the grid spacing decreases with time when the ion beam is initially switched on,[29] consistent with the observed reduction in DI current. The grid system design, with a thick decelerator spaced far from the accelerator grid, caused the decelerator perveance limit to be reached at a beam current substantially below the corresponding accelerator limit.

The dependence of j_{dr} on η_m at the 400-h point is shown in Fig. 8. The rate becomes about 5.5×10^{-11} g cm^{-2} s^{-1} upon extrapolation to $\eta_m = 72\%$. Comparison with the operating points of Fig. 7 at both low and high η_m indicates good agreement even where data are separated by 400 h of operation. It is concluded that the effect of the additional 400 h of grid wear on the deposition rate (j_{dr}) variation with accelerator voltage was relatively minor. The DI effect was more obvious at the higher η_m because of a much lower grid erosion rate by

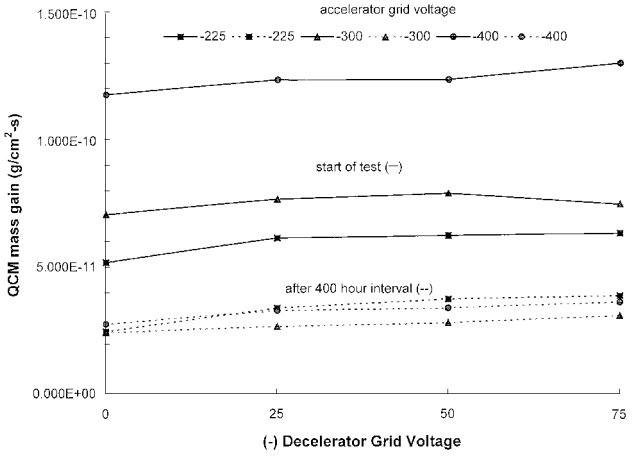

Fig. 7 Observed QCM mass deposition rate as a function of grid-extraction voltages [$\theta = 40$ deg, $I_b = 457$ mA, $V_b = 1200$ V and $\eta_m = 72\%$ at start of test (series 1); 1100 V and 90% at 400-h point (series 2), $V_{acc} = -225$ V, $V_{dec} = -50$ V].

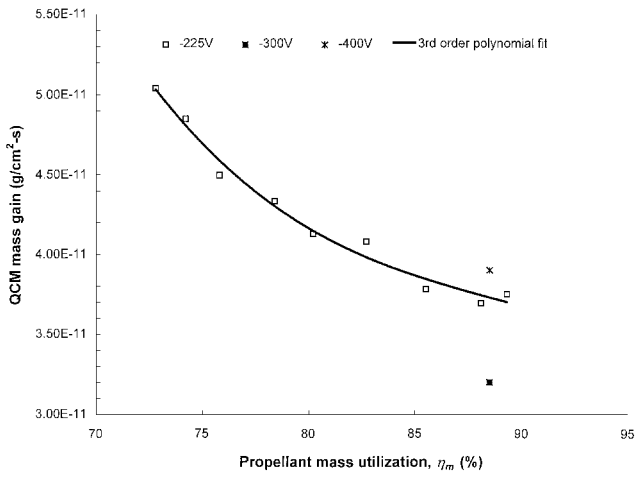

Fig. 8 Observed QCM mass deposition rate as a function of propellant mass utilization (η_m), at 400-h point (series 2), ($\theta = 40$ deg, $I_B = 457$ mA, $V_b = 1100$ V, $V_{acc} = -225$ V, $V_{dec} = -50$ V).

charge exchange ions, which resulted in a higher percentage of depositing molybdenum associated with direct impingement.

Spacecraft Materials Modification

After being exposed to the thruster-induced environment for 65 h at the operating conditions of Table 1, all 49 samples were subjected to an array of posttests, which included solar absorptance, XPS, and emittance measurements. The following relations describe fundamental relationships between materials properties examined in this study:

$$\alpha + \rho + \tau = 1 \tag{2a}$$

$$\alpha_\lambda = \varepsilon_\lambda \tag{2b}$$

For each sample, the transmittance is essentially zero, so that $\alpha + \rho = 1$, and $\varepsilon_\lambda = 1 - \rho_\lambda$. Absorptance and emittance figures for the 49 samples do not add to unity because these properties apply to different wavelength intervals; absorptance applies to the solar radiance wavelength interval, and emittance applies to the infrared wavelength interval within which the materials emit over the normal range of spacecraft temperatures. The ratio of solar absorptance to emittance is critical in determining spacecraft surface temperature.

One of the most obvious conclusions to be drawn from Fig. 9 and Table 5 is that materials with low or high initial absorptance or emittance tend to gravitate toward figures in the midrange upon exposure to the ion thruster depositional environment ($\theta = 10$–50 deg). The properties of some materials in the erosional environment (for example, $\theta = 65$ deg, where erosion rate dominates deposition rate), however, will remain virtually unchanged because of the sputter cleaning by high-velocity ions. Examples of the latter are CMX, optical solar reflector

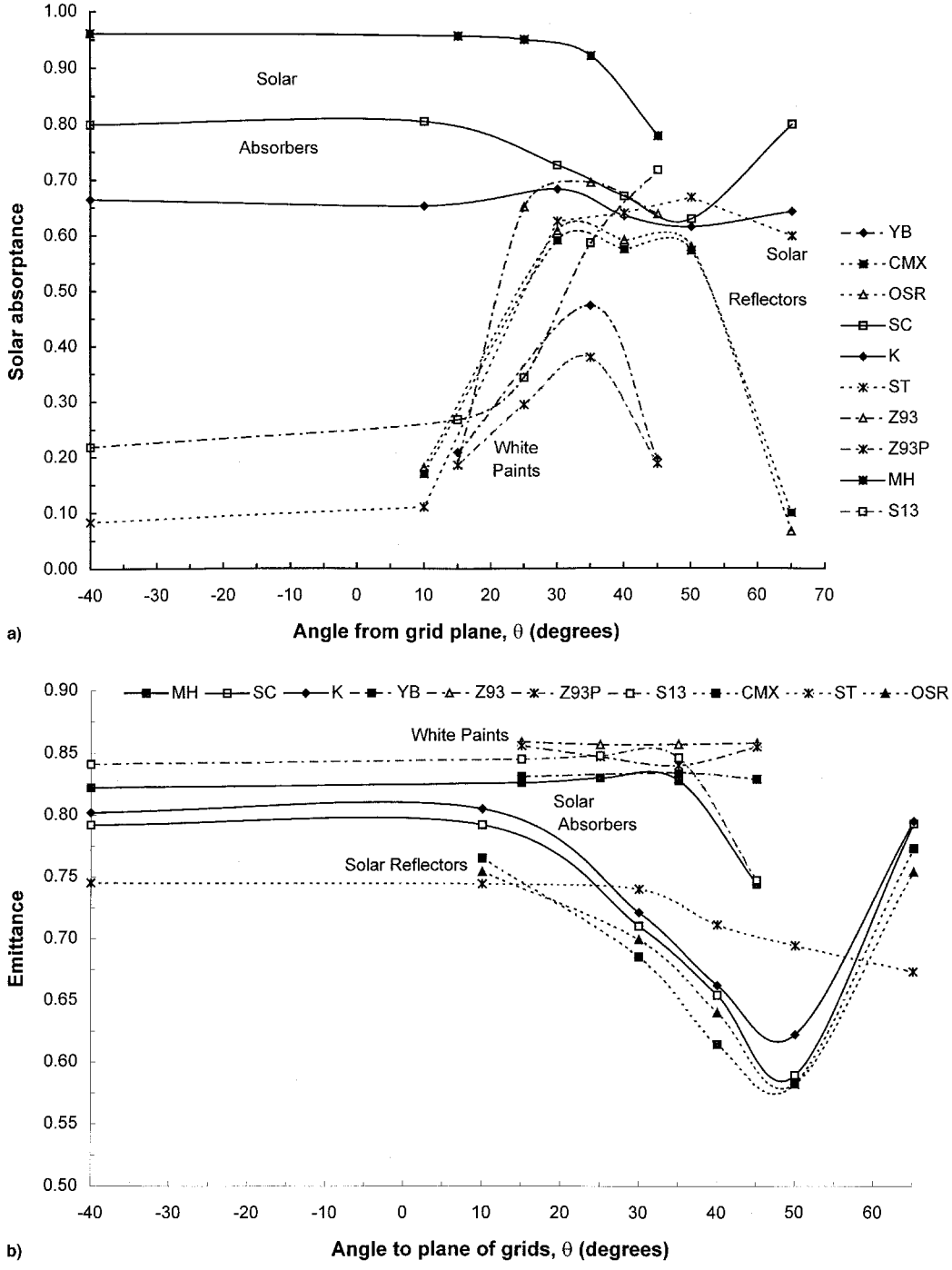

Fig. 9 a) Solar absorptance of exposed materials as a function of θ and b) emittance of exposed materials as a function of θ.

Table 5 Posttest solar absorptance and emittance measurements[a]

		Sample									
		Solar absorbers			White paints				Solar reflectors		
θ, deg	Property	MH	SC	K	YB	Z93	Z93P	S13	CMX	ST	OSR
Pretest											
	α_s	0.969	0.827	0.625	0.157	0.129	0.137	0.215	0.100	0.071	0.065
	ε_n	0.827	0.796	0.800	0.834	0.867	0.865	0.844	0.773	0.748	0.760
−40°											
	α_s	0.961	0.799	0.665	——	——	——	0.218	——	0.083	——
	ε_n	0.822	0.792	0.802	——	——	——	0.841	——	0.745	——
10											
	α_s	——	0.804	0.653	——	——	——	——	0.170	0.110	0.181
	ε_n	——	0.792	0.805	——	——	——	——	0.765	0.744	0.754
15											
	α_s	0.956	——	——	0.208	0.187	0.185	0.267	——	——	——
	ε_n	0.826	——	——	0.831	0.859	0.856	0.845	——	——	——
25											
	α_s	0.950	——	——	——	0.651	0.294	0.343	——	——	——
	ε_n	0.830	——	——	——	0.857	0.847	0.848	——	——	——
30											
	α_s	——	0.726	0.683	——	——	——	——	0.591	0.625	0.608
	ε_n	——	0.710	0.721	——	——	——	——	0.685	0.740	0.699
35											
	α_s	0.921	——	——	0.473	0.695	0.379	0.586	——	——	——
	ε_n	0.828	——	——	0.834	0.857	0.840	0.846	——	——	——
40											
	α_s	——	0.670	0.635	——	——	——	——	0.575	0.640	0.591
	ε_n	——	0.654	0.662	——	——	——	——	0.614	0.711	0.640
45											
	α_s	0.778	——	——	0.196	0.638	0.188	0.717	——	——	——
	ε_n	0.744	——	——	0.829	0.858	0.855	0.747	——	——	——
50											
	α_s	——	0.629	0.615	——	——	——	——	0.572	0.668	0.579
	ε_n	——	0.589	0.622	——	——	——	——	0.582	0.694	0.582
65											
	α_s	——	0.799	0.643	——	——	——	——	0.100	0.599	0.067
	ε_n	——	0.793	0.795	——	——	——	——	0.773	0.696	0.798

[a]Pretest results shown for comparison.

(OSR), and perhaps to a lesser degree, the solar cells and Kapton. The solar cells originally had a multilayer antireflection coating, which would eventually be lost in an erosional environment. An obvious clustering of posttest absorptance figures in the 0.65 ± 0.1 region occurs for θ = 30–50 deg. There are clearly exceptions to these behavior patterns, however.

The division of materials into solar absorber, solar reflector, and white paint classifications is a natural one, based on absorptance and emittance properties. The solar reflectors CMX and OSR, for example, show nearly identical behavior with respect to both absorptance and emittance. Their behavior with respect to emittance is also similar to that of Kapton and the solar cells. This is not the case with respect to absorptance, probably because of the large difference in initial value for the low-absorptance CMX and OSR vs the high-absorptance Kapton and solar cells.

The paints are the most complex materials from a chemical standpoint.[30,31] The white paints YB71, Z93, and Z93P have a potassium-silicate binder, whereas S13GP/LO-1 and MH21S/LO have an elastic methyl-silicone binder that makes the paint much more flexible and less susceptible to cracking. The white paints YB71 and Z93P show very similar behavior with respect to absorptance and emittance at all angles; Z93P, the less expensive paint, is slightly better despite the fact that different pigments are involved: YB71 uses zinc ortho-titanate pigment (Zn_2TiO_4) and Z93P uses ZnO.

Each paint designated with a P uses a slightly different potassium-silicate formulation because of the production shutdown of the original supplier. For example, Z93P is a recommended successor to Z93, with all aspects of their manufacturing process as identical as possible, except for the starting potassium-silicate material. The S13GP/LO-1 paint still uses a methyl-silicone binder, but the ZnO pigment is encapsulated in the new potassium-silicate formulation.

Dramatically different behavior was found between Z93 and Z93P, despite the nearly identical composition. The XPS results for these samples, discussed later, only make their contrasting behavior more mysterious. Because Z93 and Z93P were placed at adjacent stations in the sample holders, with the same angle θ, they should have experienced similar environments.

From the standpoint of smallest $\Delta\alpha$, YB71 and Z93P showed better performance than Z93 and S13GP/LO-1. The properties of the latter paints were highly degraded, except for Z93 emittance, which was very stable.

Concerning emittance, much smaller effects were determined in the posttest analyses. Figure 9 and Table 5 show that the white paints had a very small $\Delta\varepsilon$, except for S13 at 45 deg, retaining their very high emittance figures. The solar reflectors and absorbers, which had a slightly lower starting emittance, exhibited a larger $\Delta\varepsilon$. For every sample of set A, the posttest emittance was lower than the pretest figure. The QCM data of Fig. 5 indicate that the paint samples of set A, which were stationed at 45 deg, would have experienced a somewhat higher flux (the station number is considered to be insignificant, as already discussed) than the other set A materials located at 40 deg. The magnitudes of $\Delta\varepsilon$ run counter to the trend expected on the basis of flux to the samples, indicating that a material-dependent effect is likely involved. If there are indeed material-dependent effects, the paint samples might be expected to exhibit the widest variability because of their chemical complexity. There is a very large change in S13 and Z93 α_s figures, and a much smaller $\Delta\alpha_s$ for YB71 and Z93P.

Of the five materials tested at $\theta = 65$ deg, all were closer to their initial absorptance and emittance properties than the same samples at 45 or 50 deg, in spite of the deposition of sputtered Ta and Al from the collimator (see Tables 6–8). CMX was completely unchanged to within measurement uncertainty despite the complete loss of its ITO coating; OSR, Kapton, and the solar cell absorptance and emittance were very close to pretest values. However, the silver Teflon® was markedly different, particularly with respect to absorptance. The explanation for this, presumably, is that the Teflon side (the side exposed to the environment) is chemically altered by the 1100-eV ion impingement. A previous study found that 1-kV Ar^+ impingement textures the surface and can alter the properties of Teflon and Kapton, particularly the solar absorptance of the latter, at dosages $\geq 10^{18}$ ions/cm^2.[32] The relatively small change in Kapton solar absorptance in the present study may be partly a result of the much higher starting absorptance of this uncoated Kapton sample than the metal-backed film of the previous study.

It is interesting to note that each of the white paints shows the same trend toward restoration of initial property values for $\theta = 35$–45 deg, despite the higher molybdenum atom impingement rate at the higher angle (the black paint MH21S/LO does not show the same trend). This may be an indication that the ratio of metal atom sticking coefficient to sputter yield is considerably lower for the white paints than for other materials that acted essentially as sputter monitors. The impingement rate of 1100-eV xenon ions at $\theta = 50$ deg has already been discussed. The relative impingement rate at 35 and 45 deg might well explain the trend in question. Like Teflon, the paints may be chemically altered by the Xe^+ impingement, but surface cleaning will occur as well. It is unfortunate that no test of paint materials was conducted at $\theta = 65$ deg. A prior experiment involving a mercury-ion thruster did expose paint

Table 6 Solar absorbers[a]

	MH21S/LO						Solar cell							Kapton						
Atom	Pre	−40	15	25	35	45	Pre[b]	−40	10	30	40	50	65	Pre	−40	10	30	40	50	65
C	49	57	61	46	46	34	——	45	43	31	30	32	26	74	45	43	32	26	32	50
O	28	27	26	37	36	43	——	36	41	48	44	46	41	20	37	42	49	54	45	30
Si	23	8.7	11	12	12	9.6	——	1.9	4.8	3.3	2.5	0.6	6.9	——	0.6	2.2	3.1	1.9	0.8	0.3
Mo	——	0.1	1.4	4.1	4.6	8.9	——	0.1	4.8	11	14	13	4.1	——	0.1	4.8	10	9.3	14	3.4
Fe	——	——	0.4	1.1	1.2	2.5	——	0.2	4.1	4.0	5.0	5.2	1.1	——	0.1	4.0	3.6	4.5	5.2	1.3
Ni	——	——	——	——	——	——	——	——	0.4	0.3	0.2	0.7	——	——	——	0.6	0.2	0.3	0.5	——
Cr	——	——	——	——	——	——	——	——	0.4	0.4	0.7	0.3	——	——	——	1.0	0.3	0.4	0.3	——
F	——	——	——	——	——	——	——	0.4	0.5	0.8	0.9	0.5	8.1	——	0.3	0.8	0.4	——	0.5	2.3
Al	——	7.4	——	——	0.3	1.8	——	16	0.9	1.7	2.9	1.5	2.0	——	16	1.5	1.5	3.8	1.9	4.7
Mg	——	——	——	——	——	——	——	0.3	——	——	——	——	5.8	——	——	——	——	——	——	——
Ta	——	——	——	——	——	——	——	——	——	——	——	——	3.9	——	——	——	——	——	——	2.9
N	——	——	——	——	——	——	——	——	——	——	——	——	——	6.4	0.6	——	——	——	——	——

[a]Posttest XPS surface atom percent composition (normalized at indicated values of θ). Pretest figures are given for comparison.
[b]No pretest analysis, solar cells were too large for introduction into XPS. Cells were broken for postanalysis.

Table 7 White paints[a]

	YB-71/PS-7				Z93					Z93P					S13GP/LO-1					
Atom	Pre	15	35	45	Pre	15	25	35	45	Pre	15	25	35	45	Pre	−40	15	25	35	45
C	21	71	52	31	13	27	21	20	26	16	67	68	70	24	50	55	62	58	52	30
O	54	22	33	44	61	49	54	53	49	58	25	24	26	48	31	28	27	29	33	46
Si	8.4	2.6	5.9	11	13	12	13	13	12	14	2.6	0.8	0.7	13	19	15	8.7	11	10	6.6
K	10	4.1	7.0	10	6.0	8.8	9.3	9.5	9.3	7.3	5.3	5.1	0.4	10	——	——	——	——	——	——
Zn	1.9	——	0.1	0.5	7.0	——	——	0.2	1.3	4.3	——	——	——	1.4	——	——	——	——	——	——
Ti	1.9	——	——	0.2	——	——	——	——	——	——	——	——	——	——	——	——	——	——	——	——
S	2.0	——	0.3	0.3	——	——	——	——	——	——	——	——	——	——	——	——	——	——	——	——
Mo	——	0.1	0.5	1.0	——	0.4	1.1	1.5	——	——	0.5	1.1	2.5	0.7	——	——	1.0	1.3	3.3	12
Fe	——	0.3	0.6	1.0	——	1.6	1.8	2.0	1.9	——	0.3	0.1	0.6	1.0	——	——	——	——	——	3.7
Al	——	0.1	0.4	0.5	——	0.8	0.5	0.4	0.2	——	0.2	——	0.3	——	——	——	——	——	——	1.3

[a]Posttest XPS surface atom percent composition (normalized at indicated values of θ). Pretest figures are given for comparison.

Table 8 Solar reflectors[a]

	CMX (Indium–tin–oxide coated)						Silver Teflon							Optical solar reflector						
Atom	Pre	10	30	40	50	65	Pre	−40	10	30	40	50	65	Pre	10	30	40	50	65	
C	22	39	22	24	31	20	27	35	45	32	27	37	29	13	33	22	20	28	18	
O	49	45	55	53	46	47	0.4	16	34	45	49	42	7.1	59	47	56	56	51	54	
Si	0.6	2.1	2.9	1.4	——	9.6		1.1	2.0	2.5	1.5	——	——	28	2.9	2.9	2.0	0.5	16	
In	25	——	——	——	——	——	——	——	——	——	——	——	——	——	——	——	——	——	——	
Cu	2.6	——	——	——	——	——	——	——	——	——	——	——	——	——	——	——	——	——	——	
Ag	0.7	——	——	——	0.2	——	——	——	——	——	——	——	0.7	——	——	——	——	——	——	
Mo	——	6.3	12	13	16	2.5	——	0.1	4.4	9.9	11	14	1.1	——	6.8	12	12	14	3.1	
Fe	——	4.6	4.8	4.5	5.2	0.9	——	——	3.9	4.2	4.7	3.6	——	——	5.3	3.8	4.1	5.2	1.1	
Ni	——	0.4	0.3	2.5	1.2	——	——	——	0.5	0.2	0.7	0.5	——	——	0.9	0.3	0.6	——	——	
Cr	——	0.7	0.3	0.4	——	——	——	——	0.4	0.2	0.2	——	——	——	0.7	0.5	0.4	——	——	
Ta	——	——	——	——	——	2.1	——	——	——	——	——	——	1.0	——	——	——	——	——	3.0	
Al	——	1.3	2.4	2.4	0.8	3.1	——	13	1.7	1.6	1.8	0.6	0.6	——	1.8	1.7	3.8	1.3	2.9	
F	——	0.9	——	1.1	——	——	72	33	8.9	4.3	4.6	3.2	58	——	1.0	0.6	0.8	——	0.9	

[a]Posttest XPS surface atom percent composition (normalized at indicated values of θ). Pretest figures are given for comparison.

samples to a high beam-ion flux.[33] Negligible change in emittance was found, but absorptance was highly degraded above a threshold fluence of 10^{17} ions/cm^2. While this is about the same fluence of 1100-eV ions achieved at $\theta = 50$ deg in the 65-h test, xenon and mercury ions will probably affect paint properties to a significantly different extent. The fluence of charge exchange ions formed in the ion beam was higher, for most samples, than the fluence of beam ions. Because of the low energy, however, these ions would have much less effect per particle.

Tables 6–8 give the pre- and posttest XPS analysis results obtained for the various samples. Some of the materials function quite well as sputter monitors, collecting all impingement particles on the surface with minimal chemical effects. CMX, OSR, Kapton, solar cells, and silver Teflon belong to this class of materials. The second major class exhibits a strong dependence of surface-layer elemental composition on substrate in the posttest XPS results. The paints Z93, Z93P, and YB71P belong to this class (group I paints). The paints MH21S/LO and S13GP/LO-1 (group II paints) have simpler pretest and posttest chemical compositions. While group I XPS results indicate little contribution to posttest surface-layer composition derived from the thruster (molybdenum and iron being the dominant thruster efflux), group II results are much more similar to the sputter monitor results. The difference in the behavior of the three types of materials is evident in Fig. 10 and Tables 5–8. Even at the rather high molybdenum and iron flux rates in the $\theta = 30$–50-deg range, group I paints manage to limit the concentration of these atoms in the surface layer to a low level. The visible appearance of the majority of material samples changed as a result of the 65-h test (see photograph in Ref. 17).

Group I and II paints are chemically quite different.[30,31] Group I paints use a potassium-silicate binder, and have a high porosity (about 50%). Group II paints use an elastic binder, methyl silicone, and contain only carbon, oxygen, and silicon; whereas group I paints contain potassium and zinc but no carbon, plus titanium and sulfur in the case of YB71P. The two paints using the elastic binder acquire a posttest molybdenum surface atom concentration at $\theta = 45$ deg of roughly similar magnitude to the sputter monitors, in contrast to the paints with potassium-silicate binder. One possible explanation is that the elastic binder absorbs impingement energy more readily and, consequently, has a significantly lower sputtering yield and/or a higher sticking coefficient.

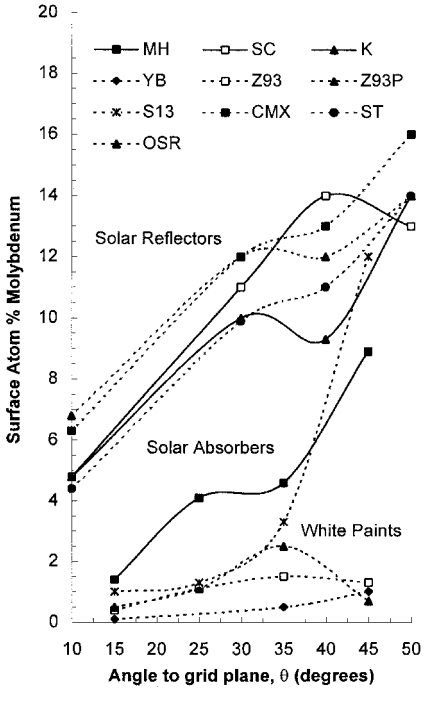

Fig. 10 Molybdenum atom abundance on the surface of exposed materials, as a function of θ.

The effects of atmospheric contamination before the 65-h test and during the interval between posttest sample removal and the performance of absorptance and emittance measurements create an element of uncertainty. Clean metals will commonly acquire a substantial surface layer containing hydrocarbons in abundance. Passivation occurs when the film is typically 15–20 Å thick. It is clear from the XPS results that substantial amounts of carbon are acquired by the samples (hydrogen is virtually invisible to XPS). For the sputter monitors, as well as MH21 and S13, the molybdenum–iron deposit from the thruster at $\theta = 40$–50 deg is deep enough (greater than 50 Å) that very little signal contribution is obtained from the underlying substrate. These samples have surface atom percentages of about 30, 45, and 14 for carbon, oxygen, and molybdenum, respectively. The vast majority of carbon atom signal presumably comes from the top 20 Å. For $\theta = 10$ and -40 deg, the carbon percentage is considerably higher because of the contribution from the underlying substrate.

Of the five materials tested at $\theta = -40$ deg, all showed very small or negligible changes in absorptance and emittance. The XPS analysis indicated the presence of substantial levels of aluminum (from the beam stop) on all samples with the exception of the only white paint tested at -40 deg, S13GP/LO-1. S13 and the other paint tested at this angle, MH21, showed no measurable property changes. It is believed that the small deltas in absorptance and emittance observed at $\theta = -40$ deg for Kapton, silver Teflon, and the solar cell were a result of the deposit of aluminum from the beam stop. Contamination was inevitable on part of each sample, despite the collimation used, because of the sample positioning behind the thruster with a partial view of downstream surfaces.

Aluminum was also found on most samples positioned at $\theta = 10$–40 deg. It is believed this was a result of the deposition of sputtered Al from the beamstop on thruster grids followed by resputtering and deposition on the collimated samples.

The vast majority of paint samples showed an increase in carbon surface atom percentage after the 65-h test. The exceptions were the elastic binder paints, MH21 and S13, at the higher values of θ, where a substantial layer of molybdenum had collected. For these samples, the XPS signal is primarily a result of the metal deposit and an atmospheric hydrocarbon adsorption layer, just as for the sputter monitors (Z93, Z93P, and YB71 pretest samples did not have a metallic deposit layer or internal carbon. Nevertheless, XPS analysis indicated 13, 16, and 21% surface carbon atoms, respectively, from adsorbed atmospheric species). MH21 and S13 at the lower values of θ showed small increases over the pretest levels of about 50%. Two paints, Z93P and YB-71, showed a dramatic increase in carbon surface atom percentage from a low pretest value (for example, the Z93P posttest percentage was about 70 at $\theta = 15$, 25, and 35 deg with a pretest value of 16%). This effect was accompanied by a large decrease in K and Si surface abundance, and an increase in the K:Si ratio. The ratio increased slightly for the other paint with potassium silicate binder, Z93, with an increase in K surface abundance. A similar trend in the K:Si ratio has been observed in a study of uv/electron irradiation of these paints.[31] It was postulated that K^+ ions migrate to the negatively charged test sample surface, aided by surface heating. The same explanation can be applied in the present case, where negative surface charges and localized surface heating can also be expected. The irradiation study established that substantial batch dependence occurs regarding response to uv/electron impingement. The Z93 posttest analysis of that study showed similar trends to the present posttest analysis of Z93P. It was suggested that low levels of organic impurities might exist in the paints that extract pigment oxygen during irradiation, thereby darkening the paint, and that the

increase in surface carbon probably resulted from the cracking of adsorbed molecules under the uv/electron flux.

It is noteworthy that the two paints showing large increases in carbon atom surface abundance, Z93P and YB-71/PS-7, use the new and old silicate formulations, respectively. Because Z93 exhibited very different behavior with respect to carbon abundance, and like YB71 uses the older formulation, the silicate can be eliminated as a source of explanation. Zinc abundance decreased dramatically for all three paints, starting from a rather low initial level, suggesting that zinc is also not responsible for the high carbon phenomenon.

The observed Z93P and YB71 low θ results are consistent with the growth of a high carbon film on top of the paint substrate. A plausible scenario is the following: the initial layer of adsorbed atmospheric hydrocarbon material becomes chemically active upon exposure to 0- to 10-eV charge-exchange Xe^+ and somewhat more energetic molybdenum and iron atom impingement. The free radicals and ions that formed react with impinging molecules containing carbon, hydrogen, and/or oxygen, most of which are produced by the 1100-eV Xe^+ bombardment of the aquadag-coated beam stop (the abundant presence of H_2, H_2O, CO, and CO_2 is routinely observed in the vacuum chamber by residual gas analysis during thruster operation). Under these conditions a carbon-rich film can grow. Because roughly 80% of the XPS signal comes from the upper 50 Å, a layer of this thickness will dramatically lower the measured surface atom percentage of substrate atoms Si, K, Zn, etc. Some of the small, positively charged potassium atoms migrate far enough toward the surface to substantially increase the XPS K:Si ratio. Carbon-rich films do not grow at $\theta = 45$ deg, because the high sputter rate for 1100-eV Xe^+ flux is high enough to prevent film growth and even remove the initial film. Film growth may be very sensitive to factors such as sample handling history. As a result, virtually identical samples with slightly different histories could produce widely varying results. Because of the relatively low surface-binding energies of paints and hydrocarbon deposits as compared to metals, the sputter yield will be considerably higher than for metals, making the transition from net deposition to net erosion occur at lower θ. While the preceding scenario seems reasonable, it leaves a number of questions unanswered.

Deposition-layer thickness on the samples, as estimated from the available XPS data, is consistent with the observed QCM rate of mass gain. A depth-profiling measurement was not made, however, and so an accurate comparison cannot be made.

Because the solar cell α_s decreased substantially with deposition-layer thickness (the measurement pertains to the combination of solar cell and deposition layer), Eq. (2a) suggests that solar reflectance may have increased significantly. Both absorptance and reflectance of the layer reduce solar cell output, and in the limit of a thick-layer transmittance to the solar cell is zero. The output of a small solar cell diagnostic array positioned near an operating mercury ion engine was observed to degrade rapidly during the SERT II mission.[9]

Grid Lifetime

The majority of mass deposition observed in this study originates from the thruster. There are two principal components: iron, from the magnetic pole pieces and stainless-steel wall of the discharge chamber, and molybdenum from the extraction grid set.

Determination of total flux of molybdenum from the thruster allows an estimate of grid and thruster lifetime, based on the accelerator grid erosion rate. Calibration of this approach would allow essentially real-time determination of grid lifetime as a function of the operating point. Reference 17 describes the details of a calculation of integrated molybdenum and iron flux based on the data presented in this report. The sum of these integrations yielded an estimated total molybdenum and iron efflux of approximately 12 and 2 g per 10,000 h, respectively, for the present case of $V_{acc} = -225$ V and $\eta_m = 0.92$. It was estimated from the data of Fig. 7 that without a decelerator DI effect the measured molybdenum flux would be reduced by about 50% at the operating point of Table 1, but this would have little effect on the accelerator grid lifetime. The value of η_m for iron efflux is not known. The T5 thruster continued to function during a lifetest despite losing about 10 g from the discharge chamber,[13] and it was concluded on the basis of these and other results[23,34] that the discharge voltage of 43–44 V in the present study, although high, is still an acceptable operating level.

It was further estimated in Ref. 17 that the central accelerator grid webbing would be completely eroded away in 10,700 $\pm$ 3000 h at the 25-mN operating point ($\eta_m \sim 90\%$). The data presented in the present report and elsewhere[35] can be used to estimate lifetime for other operating points.

Concluding Remarks

The same process that normally limits the lifetime of a gridded ion thruster, sputter erosion of the accelerator grid, is also a significant source of spacecraft contamination. Analysis of molybdenum and iron deposition rates indicates that, for a typical spacecraft configuration, slight but nonnegligible degradation of solar array output can be expected at its end of life. Slight degradation of spacecraft exterior surfaces can be expected as a result of the ion thruster. The problems facing other electrostatic ion thrusters with extraction grids are similar, although the results presented here are thruster specific.

Degradation effects may be reduced through the use of a large cant angle between thrust axis and the surface in question, and the use of a sputter shield, which would be advisable for some configurations. Means to improve grid lifetime include the use of grid materials with lower sputter yield, thruster operation at power levels well below the design capability (derating), operating at high propellant mass utilization efficiency, and varying aperture diameters across the grid radius.

Spacecraft materials would not in general be placed in the positions employed for this study (solar cells may be found at similar angles off the grid plane but at considerably greater distance). Most materials would not perform their design function there for long. Materials on the spacecraft body, aft of the grid plane, are a different matter. The test results indicate molybdenum and iron deposits that are at or below the limit of detectability for each sample at $\theta = -40$ deg. Much of what is there was probably deposited on the beam stop or other surfaces and sputtered back to these samples. These materials seem likely to perform for the mission lifetime without unacceptable thruster-induced degradation, although a more detailed investigation is desirable that includes consideration of secondary contamination transfer of solar array deposition material.

Material properties are affected by the thruster environment in a complex way that often depends upon the details of the material. Further investigation of these interactions at a fundamental scientific level would be of value.

Acknowledgments

The authors wish to acknowledge useful technical discussions with J. Pollard, S. Janson, C. Hemminger, M. Meshishnek, and G. Arnold, and the technical support of R. Ueunten and E. Yohnsee. Additional thanks to J. Pollard for modifying the software used to rotate the QCM platform; M. Meshishnek, C. Hemminger, and G. Arnold for supplying sample materials; J. Stoyack of Loral; and Y. Harada of IIT Research Institute. Special thanks to C. Hemminger for her invaluable assistance in performing materials analysis.

References

[1]Chan, A. K., Zondervan, K. P., and Smith, W. B., "Solar Electric Propulsion Assessment," The Aerospace Corp., TOR-93(3501)-2, El Segundo, CA, Dec. 1993.

[2]Fearn, D. G., "Ion Propulsion—A Technology for Improving the Cost-Effectiveness of Large Communications Satellites," *Electronics and Communication Engineering Journal*, Vol. 4, No. 3, 1992, pp. 153–162.

[3]Vaughan, C. E., and Cassady, R. J., "An Updated Assessment of Electric Propulsion Technology for Near-Earth Space Missions," AIAA Paper 92-3202, July 1992.

[4]Janson, S. W., "The On-Orbit Role of Electric Propulsion," AIAA Paper 93-2220, June 1993.

[5]Pollard, J. E., Marvin, D. C., Janson, S. W., Jackson, D. E., and Jenkin, A. B., "Electric Propulsion Flight Experience and Technology Readiness," AIAA Paper 93-2221, June 1993.

[6]Lightner, E. B., and O'Neal, R. L., "Long Duration Exposure Facility—A General Overview," NASA CP-3134, June 1991.

[7]Hall, D. F., Newman, B. E., and Womack, J. R., "Electrostatic Rocket Exhaust Effects on Solar-Electric Spacecraft Subsystems," *Journal of Spacecraft and Rockets*, Vol. 7, No. 3, 1970, pp. 305–312.

[8]Byers, D. C., "Electron Bombardment Thruster Field and Particle Interfaces," *Journal of Spacecraft and Rockets*, Vol. 16, No. 5, 1979, pp. 289–301.

[9]Kerslake, W. R., and Ignaczak, L. R., "Development and Flight History of SERT II Spacecraft," *Journal of Spacecraft and Rockets*, Vol. 30, No. 3, 1993, pp. 258–290.

[10]Nagano, H., Kajiwara, K., Gotoh, Y., Nishida, E., and Fujita, Y., "On-Orbit Performance of ETS-VI Ion Engine Subsystem," International Electric Propulsion Conf., Paper 95-139, Sept. 1995.

[11]Bassner, H., Berg, H.-P., Kukies, R., and Muller, H., "Flight Test Results of the RITA Experiment on EURECA," International Electric Propulsion Conf., Paper 93-102, Sept. 1993.

[12]Ashley, S., "Electric Rockets Get a Boost," *Mechanical Engineering*, Vol. 117, No. 12, 1995, pp. 61–65.

[13]Martin, A. R., Banks, C. R., Eaton, R. W., Hurford, P., Moulford, W. E. F. L., and Pearce, A. J., "Erosion Measurements for Two- and Three-Grid Ion Thruster Extraction Systems," International Electric Propulsion Conf., Paper 93-171, Sept. 1993.

[14]Fearn, D. G., "Ion Thruster Lifetime Limitations Imposed by Sputtering Processes," International Electric Propulsion Conf., Paper 93-177, Sept. 1993.

[15]Crofton, M. W., "Laser Spectroscopic Study of the T5 Ion Thruster," AIAA Paper 95-2921, July 1995.

[16]Gaeta, C. J., Matossian, J. N., Turley, R. S., Beattie, J. R., Williams, J. D., and Williamson, W. S., "Erosion Rate Diagnostics in Ion Thrusters Using Laser-Induced Fluorescence," *Journal of Propulsion and Power*, Vol. 9, No. 3, 1993, pp. 369–376.

[17]Ahmed, L. N., and Crofton, M. W., "Surface Modification Measurements in the T5 (UK-10) Ion Thruster Plume," AIAA Paper 95-2827, July 1995.

[18]Bond, R. A., "The Optimisation of the UK-10 Ion Thruster Extraction Grid System," International Electric Propulsion Conf., Paper 97-138, Aug. 1997.

[19]Gray, H., Smith, P., and Fearn, D. G., "UK Ion Propulsion System Development," *Journal of the British Interplanetary Society*, Vol. 49, No. 5, 1996, pp. 163–172.

[20]Gilmore, D. G. (ed.), *Satellite Thermal Control Handbook*, Aerospace Corp. Press, El Segundo, CA, 1994.

[21]Nelson, K. E., Luedke, E. E., and Bevans, J. T., "A Device for the Rapid Measurement of Total Emittance," *Journal of Spacecraft and Rockets*, Vol. 3, No. 5, 1966, pp. 758–760.

[22]Smith, C. A., and Jones, C. A., "Measurements Effects on Optical Property Design Values," NASA 9-18200, Feb. 1993.

[23]Pollard, J. E., "Plume Angular, Energy, and Mass Spectral Measurements with the T5 Ion Engine," AIAA Paper 95-2920, July 1995.

[24]Rosenberg, D., and Wehner, G. K., "Sputtering Yields for Low Energy He^+, Kr^+, and Xe^+ Ion Bombardment," *Journal of Applied Physics*, Vol. 33, 1962, pp. 1842–1845.

[25]Berisch, R. (ed.), "Sputtering by Particle Bombardment I: Physical Sputtering of Single-Element Solids," *Topics in Applied Physics*, Vol. 47, Springer–Verlag, New York, 1981.

[26]Kameyama, I., Monheiser, J. M., and Wilbur, P. J., "A Numerical Model of Thruster-Exhaust Plumes," International Electric Propulsion Conf., Paper 97-180, Aug. 1997.

[27]Brophy, J. R., Garner, C. E., Goodfellow, K. D., Pivirotto, T. J., and Polk, J. E., "Electric Propulsion System Technology," Jet Propulsion Lab., Rept. 92-10, Pasadena, CA, Nov. 1992.

[28]Fearn, D. G., "An Assessment of the Contamination of the Solar Arrays of a Communications Satellite by an Ion Thruster," International Electric Propulsion Conf., Paper 97-190, Aug. 1997.

[29]Pollard, J. E., and Welle, R. P., "Thrust Vector Measurements with the T5 Ion Engine," AIAA Paper 95-2829, July 1995.

[30]Harada, Y., "Space-Stable Thermal Control Coatings," NASA/Marshall Space Flight Center Contract NAS8-31906, Rept. IITRI-M06020-62, July 1982.

[31]Meshishnek, M. J., Hemminger, C. S., and Gyetvay, S. R., "Space Environmental Exposure of IITRI White Thermal Control Paints," The Aerospace Corp., Rept. ATM-95(5904-44)-2, El Segundo, CA, Feb. 1995.

[32]Mirtich, M. J., and Sovey, J. S., "Optical and Electrical Properties of Ion Beam Textured Kapton and Teflon," NASA Lewis Research Center, TM-73778, Cleveland, OH, 1977.

[33]Kelley, L. R., Luedke, E. E., and Hall, D. F., "Damage of Thermal Control Coating Properties by Energetic Mercury Ion Bombardment," AIAA Paper 72-445, April 1972.

[34]Mundy, D. H., "T5 Ion Engine Plume Analysis Using a Time of Flight Mass Spectrometer," International Electric Propulsion Conf., Paper 97-096, Aug. 1997.

[35]Crofton, M. W., "Evaluation of the United Kingdom Ion Thruster," *Journal of Spacecraft and Rockets*, Vol. 33, No. 5, 1996, pp. 739–747.